The Astrophysical Journal, 836:124 (13pp), 2017 February 10 doi:10.3847/1538-4357/836/1/124

Discovery and Precise Characterization by the MEarth Project of LP 661-13, an Eclipsing Binary Consisting of Two Fully Convective Low-mass Stars

Jason A. Dittmann[1], Jonathan M. Irwin[1], David Charbonneau[1], Zachory K. Berta-Thompson[2,3,6], Elisabeth R. Newton[1,4,5], David W. Latham[1], Christian A. Latham[1], Gilbert Esquerdo[1], Perry Berlind[1], and Michael L Calkins[1]
[1] Harvard-Smithsonian Center for Astrophysics, 60 Garden Street, Cambridge, MA, 02138, USA
[2] Massachusetts Institute of Technology, Cambridge, MA 02138, USA
[3] University of Colorado, 389 UCB, Boulder, CO 80309, USA
[4] Massachusetts Institute of Technology, 77 Massachusetts Avenue, Cambridge, MA 02139, USA
Received 2016 September 6; revised 2016 November 29; accepted 2016 December 7; published 2017 February 13

Abstract

We report the detection of stellar eclipses in the LP 661-13 system. We present the discovery and characterization of this system, including high-resolution spectroscopic radial velocities and a photometric solution spanning two observing seasons. LP 661-13 is a low-mass binary system with an orbital period of $4.7043512^{+0.0000013}_{-0.0000010}$ days at a distance of 24.9 ± 1.3 parsecs. LP 661-13A is a $0.30795 \pm 0.00084\,M_{\odot}$ star, while LP 661-13B is a $0.19400 \pm 0.00034\,M_{\odot}$ star. The radius of each component is $0.3226 \pm 0.0033\,R_{\odot}$ and $0.2174 \pm 0.0023\,R_{\odot}$, respectively. We detect out-of-eclipse modulations at a period slightly shorter than the orbital period, implying that at least one of the components is not rotating synchronously. We find that each component is slightly inflated compared to stellar models, and that this cannot be reconciled through age or metallicity effects. As a nearby eclipsing binary system, where both components are near or below the full-convection limit, LP 661-13 will be a valuable test of models for the structure of cool dwarf stars.

Key words: binaries: eclipsing – solar neighborhood – stars: fundamental parameters – stars: individual (LP 661-13) – stars: low-mass

Supporting material: machine-readable table

1. Introduction

The M dwarf spectral sequence spans a large range of mass, from $0.6\,M_{\odot}$ at the earliest spectral types down to the main-sequence turn off at approximately $0.08\,M_{\odot}$. This mass range spans important transitions in the physical structure of the interior of these stars. Notably, these stars transition to the fully convective regime midway through the spectral sequence, at $0.35\,M_{\odot}$ (Chabrier & Baraffe 1997). These transitions must be accurately captured in stellar models and their effect on the equations of stellar structure must ultimately be reflected in the temperatures and radii of these stars. However, the fundamental properties of low-mass stars remain a significant challenge for stellar structure models, particularly below 0.35 solar masses (Torres 2013; Baraffe et al. 2015).

Testing the mass–radius relation for low-mass stars is traditionally done through the study of eclipsing binary (EB) systems. Precise radial velocity (RV) measurements taken throughout the orbit are sensitive to the component masses of the system, while measurements of the eclipse depths and shapes are sensitive to the radii of the eclipsing stars. The best-observed, detached, double-lined EBs can provide measurements accurate at the 1% level, allowing these systems to become strong tests of current stellar models (Torres et al. 2010).

One of the closest and most well studied EB systems is CM Draconis (CM Dra). CM Dra is an eclipsing M dwarf binary at a distance of 14.5 parsecs from the Sun (Eggen & Sandage 1967; Lacy 1977). CM Dra also contains a white dwarf at a wide separation from the M dwarf pair. As instrumentation and modeling have improved, the masses and radii of the two M dwarfs are now measured at the 0.5% level (Metcalfe et al. 1996; Morales et al. 2009). Both stars in the CM Dra EB are spectral type dM4.5 with masses of 0.23 and 0.21 solar masses and radii of 0.25 and 0.24 solar radii and orbit in a 1.7 day orbit (Morales et al. 2009). The radii of these stars are inflated at the 5%–7% level (Morales et al. 2009), and this remains a problem even with the latest stellar models (Baraffe et al. 2015).

This problem is not restricted to a handful of systems. Taking only the most well-measured EB systems in aggregate, low-mass stars tend to be inflated in radius and cooler in temperature than stellar models predict (Torres 2013). The number of low-mass stars with stellar radii measured through interferometry is low (Boyajian et al. 2015), and they often do not have any direct means to measure a precise mass. High-precision measurements of stellar masses and radii for individual stars are obtained through measurements of EB light curves and radial velocities (RVs). Photodynamical analyses of recently discovered triple systems (such as KOI-126, Carter et al. 2011 and Kepler-16, Doyle et al. 2011) allow even more accurate physical parameters measurements than classical eclipsing binaries due to the presence of eclipses between all three members of the system. However, since the eclipse probability and the probability of detection are strong functions of orbital separation, these systems tend to be dominated by close-in binaries. This makes them more susceptible to the effects of tidal forces between the stars and makes them likely to be tidally locked, preventing the stars from spinning down over their lifetime. This effect makes it more likely for these systems to be magnetically active and to remain significantly magnetically active over their main-

[5] NSF Astronomy and Astrophysics Postdoctoral Fellow.
[6] Torres Fellow.

sequence lifetimes. If magnetic activity can significantly affect the interior structure of low-mass stars, then this can create an observational bias in the observed radii of these stars, especially if these effects are not accounted for in models.

Theoretical work investigating the effect of magnetic activity and star spots as solutions to the radius-inflation problem has had mixed success. Magnetic activity may cause stars to inflate in order to maintain a constant energy flux at the stellar surface because star spots are dimmer than the magnetically inactive portions of the surface (Mullan & MacDonald 2001; MacDonald & Mullan 2012). However, in order to explain the total radius discrepancy that is observed in these stars, the magnetic-field strength in the stellar interior must be on the order of 1–50 MG (Feiden & Chaboyer 2014b). It is unlikely that fields of this strength are stable in the fully convective interior of these stars (Feiden & Chaboyer 2014b), though a magnetic-field-only explanation may be able to explain the radius inflation for larger mass M dwarfs, which still possess an interior radiative zone (Feiden & Chaboyer 2014a). Ultimately, the solution to this problem may be a combination of factors all contributing to the interior structure of fully convective stars, including magnetic-field strength and activity, star-spot coverage, metallicity, and α-enhancement (Feiden & Chaboyer 2014c).

In order to probe these effects individually and in aggregate, more low-mass EB systems are needed. In particular, finding low-mass EB systems in long period orbits, where the effects of tides are negligible and the stars' magnetic activity is much weaker, is a potential way to isolate some of these factors. Then both stars in these systems essentially evolve as "single" stars. While difficult to find and follow-up, several such systems have recently been discovered and characterized. The Kepler-16 system consists of a 41-day period EB system orbited by a planet in a 229 day orbit, all exhibiting mutual occultations of each other (Doyle et al. 2011). The presence of both stellar occultations and planetary transits in this unique system allowed for extremely precise physical parameters of this system to be measured. The secondary star in the system is a $0.202\,M_{\odot}$, $0.226\,R_{\odot}$ star with a mass and radius measured with sub-1% precision. Our group has discovered a 41-day EB, LSPM J1112+7626, consisting of two M-dwarfs. These stars have masses of $M_1 = 0.395\,M_{\odot}$ and $M_2 = 0.275\,M_{\odot}$ and radii of $R_1 = 0.382\,R_{\odot}$ and $R_2 = 0.300\,R_{\odot}$ (Irwin et al. 2011). The masses of each component are measured with 0.5% precision and the radii with 1.5% precision. In addition to these long period systems, several other EB systems with low-mass stellar components have recently been found with periods in the 5–20 day range (Schwamb et al. 2013; Gómez Maqueo Chew et al. 2014; Zhou et al. 2015a). Some of the components in these systems show radii that are consistent with stellar models, while some show significant radius inflation. Assessing the cause of the radius inflation phenomenon in low-mass stars requires the discovery of sufficient numbers of these systems with sufficiently different physical characteristics (orbital separation, metallicity, etc.) as well as accurate determinations of the mass and radius of each component.

MEarth is an ongoing photometric survey of mid-to-late M dwarfs in the solar neighborhood (Distance, $D \lesssim 33$ pc), looking for low-mass rocky planets whose periods may extend into the habitable zone of their star (Nutzman & Charbonneau 2008; Berta et al. 2013; Irwin et al. 2015). The MEarth-north array in Arizona has been in operation since 2008, and a copy located in Cerro Tololo, Chile has been in operation since early 2014. By virtue of being designed to be sensitive to small planets transiting these stars, MEarth is also highly sensitive to EB systems.

Here we present the discovery of an EB system revealed during the commissioning phase of the MEarth-south array. This system shows out-of-eclipse modulations due to star spots, which change between observing seasons. Through long-term out-of-eclipse monitoring, we are able to assess the impact that transient star spots have on our ability to measure the radii of each component, which in turn allows us to more reliably probe the physical parameters of this system and assess our errors. We utilize multiple eclipse measurements with the MEarth telescopes as well as RV measurements in order to constrain the masses and radii of both components to high accuracy and test existing stellar models. In Section 2, we detail the MEarth-south array, the discovery, and the follow-up observations of this system. In Section 3, we present a joint analysis of the RV and photometric data and constrain the physical parameters of the system. In Section 4, we discuss the implications of these measurements in regards to existing theoretical stellar models.

2. Observations

2.1. The MEarth-south Observatory

MEarth-south, like its northern counterpart, consists of eight $f/9$ 40 cm Ritchey–Chrétien telescopes on German equatorial mounts. The telescopes are located at the Cerro-Tololo International Observatory (CTIO) in Chile (Irwin et al. 2015). The telescopes are automated and take data on every clear night. Each telescope is equipped with a photometer that utilizes a 2048×2048 pixel CCD with a pixel scale of approximately $0\farcs84$/pixel and a Schott RG715 glass filter with an anti-reflection coating. For information about our filter curve and photometric system, see Dittmann et al. (2016). We expect that the MEarth-south photometric system is slightly different from the north and that the results in Dittmann et al. (2016) might show minor differences with the southern array. The MEarth-south CCDs are e2v CCD230-42 devices with an NIR optimized coating with fringe suppression. We operate the MEarth cameras at -30°C, and before each exposure we pre-flash the detector. This increases the dark current (which we subtract off), but it also eliminates persistence from the previous exposure.

We gather sky flat-field frames at dawn and at dusk. Since MEarth uses German equatorial mounts, we must rotate the telescopes by 180° relative to the sky when crossing the meridian. Therefore, we take two sets of flat fields, taking adjacent pairs of flat fields on opposite sides of the meridian. This procedure also allows us to average out large-scale illumination gradients from the Sun and the Moon. This scattered light also concentrates in our detectors in the center of the field of view. The amplitude of this scattered light effect is approximately 5% of the average value of the sky across the CCD. In order to correct for this, we filter out the large-scale structure from our combined twilight flat field and use the residual flat field to track small-scale features such as inter-pixel sensitivity and dust shadows on the detector. We derive the large-scale flat-field response from dithered photometry of dense star fields.

We measure the nonlinearity of the MEarth detectors using a dedicated sequence of dome flats. At all count levels, the MEarth CCDs have a slightly nonlinear conversion of photoelectrons to data number. This nonlinearity increases

from 1%–2% at half the detector full well to 3%–4% near saturation. We correct for this effect as part of the general MEarth data reduction pipeline. Our exposure times are set to avoid surpassing 50% of the detector's full well in order to minimize this effect.

The MEarth-south target list is designed to be similar to the northern array's target list (Nutzman & Charbonneau 2008). MEarth-south observes a selection of nearby M dwarfs believed to be within 33 parsecs (pc) of the Sun and with a stellar radius of $R < 0.33\,R_{\odot}$. The completeness of the target list and the number of targets with measured parallaxes is much lower in the south than in the north because the northern target list has been assembled from a much wider array of sources. No analogous compilation existed for the southern hemisphere. For this reason, and also the availability of follow-up resources, the majority of our targets lie above $-30°$ decl., rather than being distributed uniformly across the southern sky ($\delta < 0°$). Typically, there is only one target in each MEarth-south $26' \times 26'$ field of view, with the exception of wide multiple systems and occasional unrelated asterisms. Each field is targeted individually and is selected to contain sufficient comparison stars to enable high-precision relative photometry.

Each clear night MEarth observes a set of visible target stars at a cadence of approximately 20–30 minutes. This ensures that we obtain at least two in-transit data points for a typical one-hour duration transit. If the real-time reduction software detects a potential transit (or eclipse) in-progress, standard cadence observations of other targets on that telescope are interrupted in order to perform high cadence follow-up of the potential event-in-progress (see Berta et al. 2013 for a description of the MEarth trigger). Normal operations are resumed when the event is deemed to be over or spurious and the flux from the star has returned to its normal level.

2.2. Initial Detection and Follow-up

A primary eclipse of LP 661-13 ($06^{h}56^{m}18\overset{s}{.}95$, $-08°35'46\overset{''}{.}1$; alternate names are NLTT 17194, 2MASS J06561894-0835461) was first discovered on 2014 January 28, on the second night of commissioning observations of the MEarth-south array (see Figure 1 for a finding chart for this system). Due to being in the commissioning phase, the MEarth trigger was not yet being used. Therefore, only six in-eclipse data points were taken during the event. Subsequent eclipses were observed on the nights of 2014 February 16, (primary eclipse) and 2014 February 23, (secondary eclipse), and utilized the MEarth trigger. These events, combined with out-of-eclipse monitoring in the intervening nights, allowed us to unambiguously identify the orbital period as approximately 4.704 days. Armed with the orbital period of the system, we began strategic targeting of RV observations and subsequent eclipse measurements.

We obtained RV measurements with the Tillinghast Reflector Echelle Spectrograph (TRES) on the 1.5 m Tillinghast reflector located at the Fred Lawrence Whipple Observatory (FLWO) on Mt. Hopkins, Arizona. We used the medium ($2\overset{''}{.}3$) fiber, which yields a resolving power of $R = \frac{\lambda}{\Delta\lambda} = 44{,}000$. We obtained 14 observations of LP 661-13 with TRES, with eight exposures taken in the 2014 observing season (2014 February 18–2014 March 28) and six taken in the 2015 observing season (2014 December 27–2015 January 06). Total exposure times were 1 hr per observation, except for one exposure that was 40 minutes. We obtained Thorium-Argon (ThAr) wavelength calibration exposures both before and after each science exposure. These wavelength calibration exposures were obtained with the same fiber as the one used to take the data on the target itself.

Follow-up photometric observations of both primary and secondary eclipses were performed with the MEarth-south telescopes. We observed 11 unique eclipse events with six different telescopes. In addition to the observations of individual eclipses, we monitored the brightness of LP 661-13 out-of-eclipse on each clear night from CTIO in order to assess the variability of the system due to the stellar rotation of each component bringing star spots into and out of view. We have obtained 9173 individual observations of LP 661-13, with 5098 observations being in-eclipse measurements and 4075 out-of-eclipse measurements.

3. Analysis

3.1. Spectroscopy

We reduced our TRES spectroscopic data using the procedure of Buchhave et al. (2010), the standard pipeline for RV analysis with TRES. Once these data are reduced, we use a two-dimensional cross-correlation algorithm TODCOR (Zucker & Mazeh 1994), which uses user-given templates to match each component in the system, derive their radial velocities, and measure their light ratio in the observed spectral bandpass. For both components, we used a single epoch observation of Barnard's star (GL 699) taken on 2011 April 18 as our template. Barnard's star has a spectral type of M4 (Kirkpatrick et al. 1991), and is suitable for both stars in this analysis. We also performed a reduction using the later type Wolf 359 as a template. Both templates produced consistent results, but we found the Barnard's star template to yield more precise results, as these stars are more similar to Barnard's star. We correlated our spectra using the wavelength ranges of 8270–8430 Å (aperture number 41). This region contains molecular features, which produce strong correlations and are able to robustly identify both components in the spectrum.

First, we fit for the radial velocities for both components while letting the light ratio of the two components be a free parameter in the TODCOR model. We let the light ratio vary between each observation. The light ratio is determined by the ratio of the strengths of the features in the spectrum for each component, after matching to the stellar template (in this case, Barnard's star). Once we obtained an initial solution for each epoch, we averaged the fitted light ratio for each epoch. We then fixed the light ratio to this value and re-derived the best-fit radial velocities for each component. We find a best-fitting light ratio of $L_2/L_1 = 0.434+/-0.025$. Using the derived physical parameters for our system, the temperature scale of Mann et al. (2015), and the models of Allard et al. (2001), we predict a light ratio of $L_2/L_1 = 0.406$ for this system at these wavelengths, consistent with what we measure through our high-resolution spectra. We do not use this light ratio when fitting our photometry.

We report the radial velocities from this analysis in Table 1 and show a plot of the heliocentric radial velocities in Figure 2. We omit one observation taken on BJD 2456743 because we could not resolve both components in the spectrum due to their proximity in velocity space for this epoch and the likelihood that the primary peak would be systematically skewed in velocity due to the unresolved secondary peak in the cross-correlation. We estimate the uncertainty of our velocities

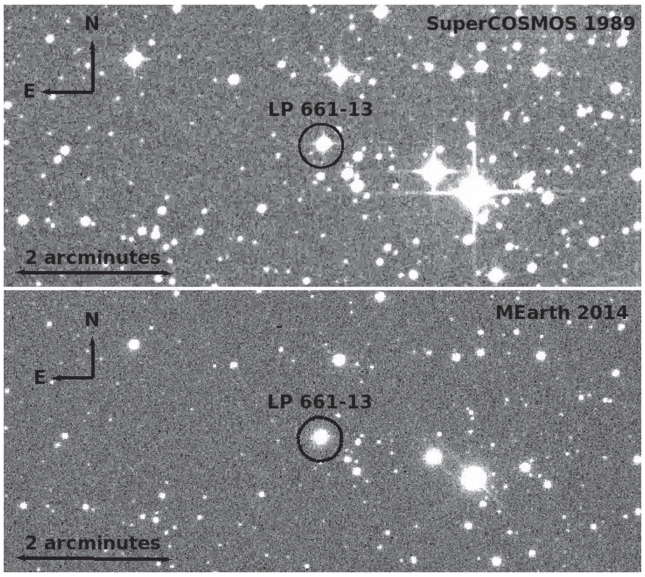

Figure 1. Finding chart for LP 661-13. The top image is archival data taken by the SuperCOSMOS survey from 1989. The bottom image is an MEarth image taken in 2014. The circle does not represent the MEarth aperture; its size is selected for clarity. The SuperCOSMOS image indicates that there is a faint background star that currently sits in the MEarth aperture for LP 661-13. We address this third-light contamination later in the text.

Table 1
TRES Radial Velocities for LP 661-13 (Barycentric)

Date (HJD)	v_1 (km s^{-1})	v_2 (km s^{-1})
2456706.708137	−38.974	61.767
2456709.709816	26.444	−41.731
2456738.656903	−8.507	13.448
2456740.665846	−9.123	14.699
2456741.701681	35.657	−56.743
2456742.704103	23.730	−37.638
2456744.696853	−35.311	56.147
2457018.893616	23.966	−38.260
2457019.845650	36.549	−58.105
2457020.921800	−8.778	14.120
2457025.844636	−19.396	30.542
2457026.835799	−37.595	59.583
2457028.858941	38.496	−61.060

(based on the standard deviation of our residuals) as 0.05 km s^{-1} for the primary and 0.20 km s^{-1} for the secondary. We assume a barycentric velocity for Barnard's star of -110.506 ± 0.035 km s^{-1} (Nidever et al. 2002), and derive a barycentric velocity for this system of -0.009 ± 0.037 km s^{-1}, including both our internal uncertainty in the barycentric velocity of the system and the error in the determination for Barnard's star (see modeling Section 4 for a description of how we obtained this quantity.).

3.2. Photometry

We measure stellar positions using a method similar to Irwin (1985). We estimate the local sky background by binning each image in 64 × 64 pixel blocks and measure the peak of the histogram of the intensity of these pixels. This lower-resolution map is then interpolated to measure the background level anywhere in the image. Sky background is estimated with a sky annulus between 18 and 24 pixels away from the stellar photo

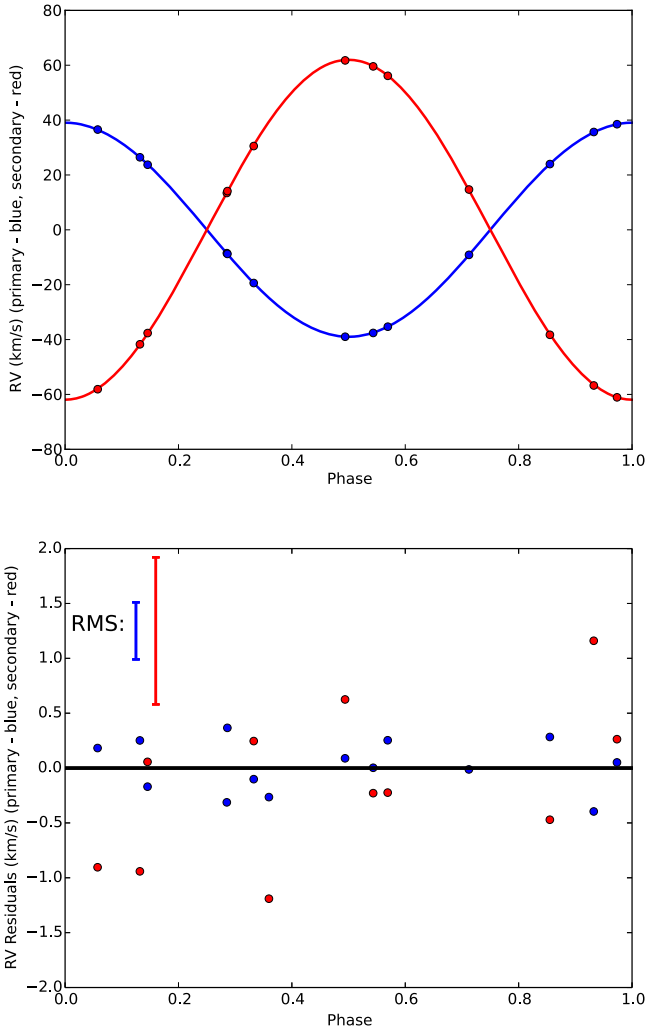

Figure 2. Top: radial velocity signal from each component of LP 661-13. The primary component is in blue and the secondary component is in red. We find a primary mass of $M_1 = 0.3057 \pm 0.0032\,M_\odot$ and $M_2 = 0.1930 \pm 0.0014\,M_\odot$ orbiting with a period of $P = 4.7043518^{+0.0000017}_{-0.0000014}$ days. Bottom: residuals from the fit. We find an rms precision of 0.05 km s^{-1} for the primary component and 0.20 km s^{-1} for the secondary component.

center. We measure stellar locations from the intensity weighted first moment (i.e., the centroid) of the star.

We measure the total flux using a 6 pixel (≈5.″04) aperture radius. We weight pixels that lie partially within this circular aperture by the fraction of the pixel that lies within the ideal circular aperture. We also adopt an aperture correction to correct for the stellar flux that falls outside of our aperture. The typical size of an aperture correction is 0.04 magnitudes, but can vary from night to night depending on atmospheric conditions (predominantly seeing). In Table 2, we provide the corrected photometry for LP 661-13 across all telescopes and both seasons of data.

There is a marginal *Roentgan Satellite* (*ROSAT*) detection in the *ROSAT* faint source catalog (Voges et al. 2000). The potential source has a count rate of $3 \pm 1 \times 10^{-2}$ counts per second. This corresponds to a flux density of approximately $1.70 \pm 0.56 \times 10^{-13}$ erg cm^{-2} s^{-1}. While this may be interesting to assess the significance of the X-ray emission with stellar activity and radius inflation, further X-ray data to confirm this potential detection are needed.

Table 2
MEarth Photometry for LP 661-13

Date (HJD)	Δ magnitude	Error (mag)	Telescope
2456685.55228	−0.0012	0.0020	tel15
2456685.55287	−0.0003	0.0020	tel15
2456685.56806	−0.0006	0.0019	tel15
2456685.56866	−0.0014	0.0019	tel15
2456685.58610	−0.0031	0.0019	tel15

(This table is available in its entirety in machine-readable form.)

3.3. Astrometry

With two seasons of photometric data from the MEarth observatory, we are able to utilize the MEarth astrometric pipeline to measure the trigonometric distance to LP 661-13. The astrometric pipeline is described in detail in Dittmann et al. (2014), but we summarize it here. We eliminate nights for which the full width at half maximum for the image is greater than 5 pixels (approximately 3.5 arcseconds), or the average ellipticity of the target stars is greater than 0.5 (typically due to wind shake). We also eliminate images for which the pointing on the image is more than 15 pixels discrepant from the master MEarth image. We fit each image with a linear model in both the x and y coordinates, which allows for translation, rotation, shearing, and pixel scale variations. We also include a separate constant offset between data taken on opposite sides of the meridian, to accommodate the image flip that results from the telescopes' German equatorial mount.

We choose reference stars that lie within 600 pixels of the target star to avoid higher order effects at the edges of the CCD. We fit our astrometry iteratively, first fitting the linear plate model to each frame and then fitting for the proper motion and parallax of each star until convergence. Internal errors are estimated through a residual permutation. This provides the advantage that it preserves time-correlated noise in our error assessment but tends to be a weaker way to estimate errors for series with few data points. However, we have over 9000 data points and do not believe our astrometric error bars are underestimated.

We perform our astrometric analysis for only the telescope that has the largest number of data points over the largest time baseline. This time baseline ensures that we can resolve any degeneracies between the proper motion and the parallax of the star. Using only one telescope eliminates possible systematics with combining data from multiple telescopes. Additionally, observations from other telescopes were targeted observations of eclipses and are of little use for astrometric analyses, which require data to be taken over the Earth's entire orbit. We show our astrometric time series in Figure 3, and measure a trigonometric parallax of $\pi = 40.2$ milliarcseconds (mas) with an internal error of 1.0 mas. However, since MEarth-south astrometry has not been benchmarked to a sample of stars with previously measured parallaxes (unlike MEarth-north), we inflate this error bar by a factor of two to be conservative. This corresponds to a distance of $D = 24.87 \pm 1.3$ parsecs (pc). We do not calculate a correction from relative parallax to absolute parallax, as this effect is smaller than our errors. We find proper motions of 75.1 ± 2.0 mas yr^{-1} in the R.A. direction and -227.3 ± 2.0 mas yr^{-1} in the decl. direction, where we have also inflated our internal error bars in the same manner as for the parallax amplitude. These values are consistent with the proper motion of 76.9 ± 5.5 mas yr^{-1} in the R.A. direction and -219.6 ± 5.5 mas yr^{-1} previously reported by Salim & Gould (2003).

4. System Modeling

We model this system following a similar procedure as Irwin et al. (2011). While for LSPM J1112+7626 Irwin et al. (2011) notes that the system is eccentric and therefore the photometric and spectroscopic solutions are highly interrelated, for LP 661-13 we find no detectable eccentricity, and so the analysis is made simpler. We model the system using the light-curve generator from JKTEBOP[7] (Southworth et al. 2004; see Southworth 2013 for the most recent version). JKTEBOP is based on the EB program EBOP (Popper & Etzel 1981). We use a modified version derived from Irwin et al. (2011), which computes the integrals analytically using the method of Mandel & Agol (2002) and its erratum.

The out-of-eclipse light-curve modulation indicates that there is significant spot activity on the surface of at least one component of the system, possibly both. This complicates the analysis because star spots have the capability of causing systematic errors in the measurement of the stellar radii as well as the surface brightness ratio of the two components, which is derived from the eclipse depths. Spots, when occulted during the eclipse, reduce the observed depth of the eclipse relative to a non-spotted star, since a relatively dimmer portion of the star is being occulted. Conversely, the presence of non-occulted spots systematically increases the eclipse depth because the eclipse is preferentially obscuring brighter portions of the star. In reality, it is likely that both occulted and unocculted spots exist in any given eclipse. It is extremely difficult to infer the true spot distribution of a system, except in cases where eclipse deviations (i.e., spot crossing events) are readily distinguished in the light curve. Out-of-eclipse modulations can help assess spot coverage but are sensitive to only the longitudinally asymmetric distribution of star spots. A uniformly spotted star would show no variation at all because a star spot rotating out of view would be replaced by an identical spot rotating into view. Identifying, or failing to identify, multiple frequencies in the out-of-eclipse modulations can also help determine whether the star spots are concentrated on one star or if both components display significant asymmetric spot coverage; though, if only one period in the out-of-eclipse modulation is detected, it is impossible to determine on which component the signal originates. We note that the eclipses in this system are grazing eclipses, not total and that there are stellar latitudes that are excluded from the eclipse geometry. Any star spots located on these latitudes cannot be mapped via these eclipses and we are insensitive to any direct measurements at these latitudes. Only longitudinal asymmetries at these latitudes are directly observable via rotational modulation. We note that it is impossible to know the true distribution of star spots on the stellar surface. There are stellar latitudes in this system that will remain unprobed. Furthermore, due to the comparable size of the stars in this system, eclipse-mapping star spots through successive eclipses does not provide significant resolution on the stellar surface and rotational modulation is only sensitive to longitudinally asymmetric distributions of star spots. However,

[7] See http://www.astro.keele.ac.uk/jkt/codes/jktebop.html for the original JKTEBOP code.

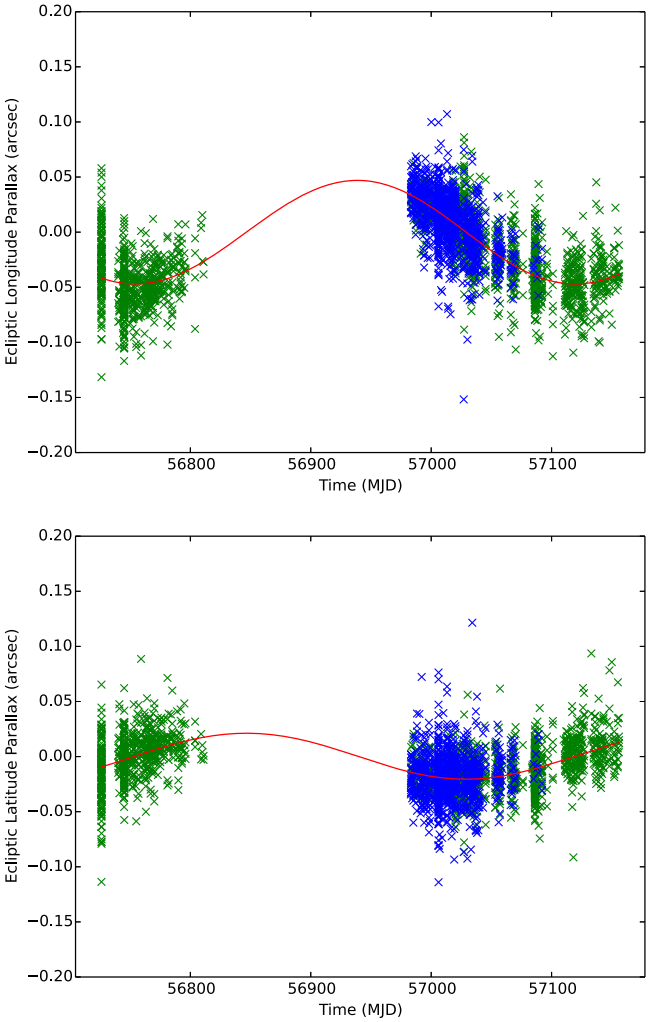

Figure 3. Trigonometric parallax signal from MEarth-south images in ecliptic longitude (left) and ecliptic latitude (right) for LP 661-13. We follow the procedure of Dittmann et al. (2014) because MEarth-south and MEarth-north were built to be nearly identical arrays. We find a parallax of $\pi = 40.2 \pm 2.0$ mas, which corresponds to a distance of 24.87 ± 1.3 parsecs. Each color represents data taken on opposite sides of the meridian. Since the MEarth telescopes are situated on German equatorial mounts, when they cross the meridian they must rotate 180°. This creates an astrometric offset between data taken in these configurations due to flexure in the instrument, which we correct with an offset. See Dittmann et al. (2014) for further discussion of the MEarth astrometric pipeline.

we attempt to parameterize and explore the effect of star spots on our measurements in this work.

We adopt the spot model from Irwin et al. (2011), which assumes that the out-of-eclipse modulations are solely due to star spots, and assumes a simple sinusoidal form for the modulations. The functional form for these modulations is

$$\frac{\Delta L_i}{L_i} = a_i \sin\left(\frac{2\pi F_i t}{P}\right) + b_i \cos\left(\frac{2\pi F_i t}{P}\right) - \sqrt{a_i^2 + b_i^2} \quad (1)$$

where t is the time, L is the light from the star, i denotes each component of the system, a_i and b_i are the constants expressing the amplitude and the phase of the out-of-eclipse modulation, and F_i is the ratio of the rotational frequency of the star to the orbital frequency.

In the present case, we find only one significant period for the out-of-eclipse modulations. However, since the observed modulation has a period close to the orbital period of the system, it is possible that both stars have similar periods and that they are close to a tidal locking scenario. This means that we cannot be sure on which component the star spots originate, and we must account for this systematic uncertainty. Unfortunately, fitting a spot model on both components is degenerate, given the limited information available from a single modulation derived from total integrated light measurements. In order to assess the full range of possible physical parameters that are consistent with the data, we fit a series of models with different spot parameters.

We use two parameters to describe the effects of star spots in our model—the fraction of eclipsed spots and the base spottedness of the star. In Section 4.3.3 of Irwin et al. (2011), it was found that the fraction of eclipsed spots does not affect the radii or the light ratio of the components and only affects the surface brightness ratio. Adding "non-eclipsed" spots affects the light ratio and the radii, but not significantly. However, we reiterate here that this is a mathematical formalism of the effect of spots, and not a physical model describing a real star-spot distribution on the star. We assess the possible systematic effects of this model choice later in this section, but state here that these effects are important at approximately the 1.5% level.

We fit both the spectroscopic RV data and the photometric light curve (both in and out-of-eclipse) simultaneously. We give the aggregate RV data set the same statistical weight as the entire photometric data set, despite the latter having thousands more individual data points. We fix the error bars on the RV data set to their rms values. This is largely irrelevant, as the system is not eccentric and therefore the RV data and the photometric data are sensitive to independent system parameters. We assume here that there is no third light in the system; in Section 4.1, we show that third light would not significantly corrupt our estimates of the system parameters.

We fit two different models, one where there are star spots on only the primary component of the system, and one where the spots are concentrated on solely the secondary component of the system. We also fit the data from the 2014 season and the 2015 season independently and allow the star-spot modulation to change between seasons. Through this method, we aim to explore the possible effect that star-spot contamination can have on our inference of the stellar radii. We explore this parameter space using the `emcee` code (Foreman-Mackey et al. 2013), which is a python implementation of the Affine Invariant Markov Chain Monte Carlo sampler. Each model is initiated with 100 walkers in a Gaussian ball located at an approximate solution. We run the chain for 50,000 steps and discard the first 5000 steps to allow the solution to "burn-in." We use uninformative (unbound, uniform) priors for all of our model parameters, except for the limb-darkening law. Quadratic limb-darkening parameters are initiated with the model of Claret (2000) for each component utilizing an approximate temperature ($T_{\rm eff} = 3700$ K, $\log(g) = 5.0$) and the Cousins I-band filter. Each coefficient is allowed to vary freely, but not exceed a 10% deviation from this theoretical value. This allows the model to adjust for differences in the actual star compared to the theoretical parameters as well as for the slight differences between our bandpass and *Cousins I* without venturing into physically implausible parameter space. Letting the limb-darkening parameters float in this way allows us to explore our prior, and we do not contend that our results are a physical

Table 3
Model Parameters

Parameter	Value	Prior	Description
$J_{\rm MEarth}$	Varied	Uniform	Central surface brightness ratio (secondary/primary) in *MEarth*
$(R_1 + R_2)/a$	Varied	Uniform	Sum of the radius of each component divided by the semimajor axis
R_2/R_1	Varied	Uniform	Radius ratio
cos i	Varied	Uniform (isotropic in i)	Cosine of the orbital inclination
M_2/M_1	Varied	Uniform	Mass ratio
$K_1 + K_2$	Varied	Uniform	Sum of RV semi-amplitudes (km s^{-1})
$u_{1,1}$	Varied	Uniform (0.2232–0.2728)	Linear limb-darkening coefficient for primary
$u_{1,2}$	Varied	Uniform (0.5364–0.6556)	Quadratic limb-darkening coefficient for primary
$u_{2,1}$	Varied	Uniform (0.4581–0.5599)	Linear limb-darkening coefficient for secondary
$u_{2,2}$	Varied	Uniform (0.3717–0.4543)	Quadratic limb-darkening coefficient for secondary
β_1	0.32	…	Gravity darkening exponent for primary
β_2	0.32	…	Gravity darkening exponent for secondary
L_3	0	…	Third-light component divided by total system light
F	Varied	Uniform	Ratio of rotational to orbital frequency
f_1	Varied (Fixed for final solution)	Uniform	Fraction of spots eclipsed
f_2	Varied (Fixed for final solution)	Uniform	Base spottedness of star
a	Varied	Uniform	Out-of-eclipse sine coefficient
b	Varied	Uniform	Out-of-eclipse cosine coefficient
$e\cos\omega$	Varied (Fixed for final solution)	Uniform	Eccentricity times cosine of argument of periastron
$e\sin\omega$	Varied (Fixed for final solution)	Uniform	Eccentricity times sine of argument of periastron
P	Varied	Uniform	Orbital period of system (heliocentric) (days)
T_0	Varied	Uniform	Epoch of primary eclipse (HJD—2456600.0)
γ	Varied	Uniform	Barycentric systemic radial velocity of system (km s^{-1})

Table 4
Parameters for Model with Star Spots on Primary Component

Parameter	2014 Season	2015 Season
$J_{\rm MEarth}$	$0.8705^{+0.0298}_{-0.0268}$	$0.8698^{+0.0261}_{-0.0177}$
$(R_1 + R_2)/a$	$0.0574^{+0.0007}_{-0.0008}$	$0.0574^{+0.0005}_{-0.0004}$
R_2/R_1	$0.6836^{+0.1065}_{-0.1539}$	$0.7500^{+0.0674}_{-0.0717}$
cos i	$0.0425^{+0.0008}_{-0.0013}$	$0.0426^{+0.0005}_{-0.0006}$
M_2/M_1	0.6299 ± 0.0020	0.6299 ± 0.0020
$K_1 + K_2$	100.983 ± 0.077	100.983 ± 0.077
$u_{1,1}$	$0.2474^{+0.0188}_{-0.0189}$	$0.2579^{+0.0105}_{-0.0269}$
$u_{1,2}$	$0.6102^{+0.0376}_{-0.0608}$	$0.6413^{+0.0105}_{-0.0218}$
$u_{2,1}$	$0.4901^{+0.0530}_{-0.0272}$	$0.4723^{+0.0305}_{-0.0116}$
$u_{2,2}$	$0.4123^{+0.0324}_{-0.0299}$	$0.4157^{+0.0292}_{-0.0306}$
F	$1.2288^{+0.0030}_{-0.0145}$	$1.2284^{+0.0039}_{-0.0160}$
f_1	$0.0684^{+0.2328}_{-0.0473}$	$0.0561^{+0.1512}_{-0.0353}$
f_2	$0.0157^{+0.0838}_{-0.0110}$	$0.0104^{+0.0212}_{-0.0070}$
a	$0.0009^{+0.0005}_{-0.0007}$	$0.00035^{+0.00026}_{-0.00035}$
b	$-0.0003^{+0.0003}_{-0.0002}$	$-0.00016^{+0.00027}_{-0.00023}$
$e\cos\omega$	$-0.00003^{+0.00003}_{-0.00006}$	$0.000000^{+0.000017}_{-0.000038}$
$e\sin\omega$	$-0.000003^{+0.000450}_{-0.000090}$	$-0.000003^{+0.000038}_{-0.000054}$
P	$4.704364^{+0.000040}_{-0.000008}$	$4.704360^{+0.000005}_{-0.000005}$
T_0	$2456705.5602^{+0.0001}_{-0.0006}$	$2456705.5598^{+0.0003}_{-0.0003}$
γ	−0.009 ± 0.014	−0.009 ± 0.014

Table 5
Model Parameters for Star Spots on Secondary Component

Parameter	2014 Season	2015 Season
$J_{\rm MEarth}$	$0.9114^{+0.0453}_{-0.0294}$	$0.8729^{+0.0254}_{-0.0252}$
$(R_1 + R_2)/a$	$0.0580^{+0.0012}_{-0.0010}$	$0.0573^{+0.0006}_{-0.0006}$
R_2/R_1	$0.6894^{+0.1558}_{-0.0929}$	$0.7493^{+0.1297}_{-0.0722}$
cos i	$0.0430^{+0.0015}_{-0.0014}$	$0.0424^{+0.0008}_{-0.0007}$
M_2/M_1	0.6299 ± 0.0020	0.6299 ± 0.0020
$K_1 + K_2$	100.983 ± 0.077	100.983 ± 0.077
$u_{1,1}$	$0.2393^{+0.0230}_{-0.0116}$	$0.2582^{+0.0100}_{-0.0167}$
$u_{1,2}$	$0.5777^{+0.0469}_{-0.0316}$	$0.6395^{+0.0122}_{-0.0361}$
$u_{2,1}$	$0.5048^{+0.0379}_{-0.0352}$	$0.4767^{+0.0406}_{-0.0156}$
$u_{2,2}$	$0.4034^{+0.0331}_{-0.0239}$	$0.3927^{+0.0357}_{-0.0161}$
F	$1.778^{+0.0102}_{-0.4461}$	$0.9098^{+0.2803}_{-0.0052}$
f_1	$0.0193^{+0.2414}_{-0.0182}$	$0.0023^{+0.0075}_{-0.0016}$
f_2	$0.0154^{+0.0850}_{-0.0144}$	$0.0024^{+0.0105}_{-0.0015}$
a	$0.0033^{+0.0019}_{-0.0032}$	$0.0017^{+0.0037}_{-0.0021}$
b	$0.0010^{+0.0006}_{-0.0009}$	$0.00010^{+0.0038}_{-0.0039}$
$e\cos\omega$	$-0.000058^{+0.000041}_{-0.000067}$	$-0.000055^{+0.000031}_{-0.000029}$
$e\sin\omega$	$-0.00000^{+0.00181}_{-0.00069}$	$0.000013^{+0.00012}_{-0.000029}$
P	$4.70438^{+0.00002}_{-0.00001}$	$4.704362^{+0.0000051}_{-0.0000052}$
T_0	$2456705.56034^{+0.00006}_{-0.00006}$	$2456705.55972^{+0.00033}_{-0.00034}$
γ	−0.009 ± 0.014	−0.009 ± 0.014

measurement of the actual limb-darkening parameters for these stars.

In Table 3, we list the physical parameters of our model (not including the normalizations for each telescope and each eclipse), and in Tables 4 and 5 we show the resulting best-fit model and the 16th and 84th percentiles (approximately 1σ) for each parameter for each season. We are able to fit our measured light curves equally well regardless of which star we place star spots. However, if we place the star-spot signal on the secondary component, the out-of-eclipse model parameters vary significantly between observing seasons, whereas if the star-spot signal is originating on the primary component, the parameters are stable between seasons. Particularly, F, the ratio between the orbital and rotational frequency has different values for each season if the secondary component is responsible for the star-spot modulation signal. Since the rotation period of the secondary star should not change (and the effect of differential rotation for star spots at different latitudes is small for M dwarfs; Davenport et al. 2015), we conclude that the star-spot signal cannot be originating on the secondary component. Since we only detect one rotational frequency, and this frequency differs from the orbital frequency of the system, we have assumed that it is originating solely on one component

of the system (the primary component); though, in reality, there is likely to be some star spots on the surface of both components and that rotation of the secondary component may also be contributing somewhat to this signal (though we do not have a significant detection). We will utilize the model for which star spots are located on the primary component for the rest of this paper. We note, however, that this choice does not significantly affect the values of the masses and radii of the components but does change the uncertainty. The light curves themselves are most directly sensitive to the sum of the component radii and their ratio. The eclipse duration measures a combination of $(R_1 + R_2)/a$ (where R_1 and R_2 are the component radii and a is the semimajor axis) and the inclination of the orbit. In the case of grazing eclipse (where we cannot break this degeneracy with a measurement of the duration of the total phase), this degeneracy is instead broken by the eclipse depth, which also depends on the limb darkening of the stars and the star spots on the stellar surfaces.

The base spottedness and the fraction of eclipsed spots model parameters are unconstrained by the data and allowed to float to allow us to explore parameter space and assess our total uncertainty in our derived physical parameters. In order to assess possible systematic uncertainties associated with these model parameters, we also run MCMC chains holding these parameters fixed at 0.0, 0.25, 0.50, 0.75, and 1.0. We find that these parameters typically induce a 1.5% variation in the uncertainty of the radii of the component stars, and a negligible effect on the mass of the stars (which is primarily constrained with the RV data). While this systematic error is partially explored by letting these model parameters float in the chain, there will likely be some residual systematic error not captured in our MCMC runs.

For our final solution, we fit both seasons jointly, requiring the same physical parameters across seasons but allowing the star-spot model to change (but not change components). We have also fixed the fraction of eclipsed spots (f_1) to 1.0 and the base spottedness of the star (f_2) to 0.0 because it would take unlikely spot distribution on the surface of the star to significantly change these parameters. In order for the fraction of eclipsed spots to significantly deviate from 1.0, the latitudinal distribution of star spots would have to be preferentially distributed away from the eclipse chord. We also note that the the base-spottedness parameter (which describes the symmetrically distributed star-spot component) is set to 0, but does not affect the physical parameters derived for this system significantly.

See Irwin et al. (2011) for a detailed investigation of the role that these parameters play in affecting measured masses, radii, and brightness temperatures. We also fix the orbital eccentricity at 0 because we see no evidence for orbital eccentricity in this system from our eclipse timings ($e < 4 \times 10^{-4}$, 95% confidence). In Table 6, we list the final model parameters for our joint fit of both seasons of data assuming star spots distributed on the primary component, and in Table 7 we list the physical parameters, including component masses and radii, for the LP 661-13 system. In Figures 4 and 5, we show each individual primary and secondary eclipse as well as their residuals with this model. In Figure 6, we show the out-of-eclipse modulations, phase-folded to the rotational period detected in our data (we reiterate that this is not the orbital period of the system). We find a rotational period associated with the star-spot modulation of 3.856 days, slightly faster than the

Table 6
Joint Model Parameters[a]

Parameter	Value (Prim. spots, $L_3 = 0$)	Value (Prim. spots, $L_3 = 0.01$)
$J_{\rm MEarth}$	$0.9004^{+0.0037}_{-0.0085}$	$0.8933^{+0.0086}_{-0.0209}$
$(R_1 + R_2)/a$	$0.05714^{+0.00037}_{-0.00035}$	$0.05710^{+0.00045}_{-0.00038}$
R_2/R_1	$0.6745^{+0.0095}_{-0.0112}$	$0.675^{+0.038}_{-0.013}$
cos i	$0.04206^{+0.00034}_{-0.00038}$	$0.04202^{+0.00040}_{-0.00045}$
M_2/M_1	$0.634^{+0.020}_{-0.006}$	$0.6314^{+0.0082}_{-0.0080}$
$K_1 + K_2$	$100.96^{+0.14}_{-0.18}$	$100.834918085^{+0.10}_{-0.11}$
$u_{1,1}$	$0.2411^{+0.0040}_{-0.0046}$	$0.2419^{+0.0117}_{-0.0038}$
$u_{1,2}$	$0.5770^{+0.0085}_{-0.0082}$	$0.5796^{+0.0098}_{-0.0167}$
$u_{2,1}$	$0.5113^{+0.0055}_{-0.0081}$	$0.498^{+0.013}_{-0.025}$
$u_{2,2}$	$0.4140^{+0.0044}_{-0.0145}$	$0.4151^{+0.0081}_{-0.0120}$
F (season 1)	$1.226^{+0.010}_{-0.012}$	$1.205^{+0.026}_{-0.023}$
f_1 (season 1)	1 (fixed)	1 (fixed)
f_2 (season 1)	0 (fixed)	0 (fixed)
a (season 1)	$0.00137^{+0.00013}_{-0.00002}$	$0.001351^{+0.000025}_{-0.000073}$
b (season 1)	$-0.000492^{+0.000006}_{-0.000019}$	$-0.000499^{+0.000009}_{-0.000082}$
F (season 2)	$1.2300^{+0.0008}_{-0.0159}$	$1.2301^{+0.0007}_{-0.0015}$
f_1 (season 2)	1 (fixed)	1 (fixed)
f_2 (season 2)	0 (fixed)	0 (fixed)
a (season 2)	$0.00134^{+0.00002}_{-0.00014}$	$0.00134^{+0.00002}_{-0.00011}$
b (season 2)	$-0.000491^{+0.000057}_{-0.000006}$	$-0.000484^{+0.000043}_{-0.000017}$
e cos ω	0 (fixed)	0 (fixed)
e sin ω	0 (fixed)	0 (fixed)
P	$4.7043512^{+0.0000013}_{-0.0000010}$	$4.7043504^{+0.0000017}_{-0.0000014}$
T_0	$2456705.560353^{+0.000038}_{-0.000040}$	$2456705.560446^{+0.000094}_{-0.000087}$
γ	-0.009 ± 0.014	-0.009 ± 0.014

Value (Section spots, $L_3 = 0$)	Value (Section spots, $L_3 = 0.01$)
$0.891^{+0.015}_{-0.017}$	$0.891^{+0.012}_{-0.024}$
$0.05730^{+0.00035}_{-0.00031}$	$0.05710^{+0.00053}_{-0.00031}$
$0.679^{+0.033}_{-0.018}$	$0.678^{+0.028}_{-0.010}$
$0.04218^{+0.00039}_{-0.00037}$	$0.04189^{+0.00054}_{-0.00023}$
$0.6320^{+0.0081}_{-0.0048}$	$0.632^{+0.012}_{-0.013}$
$100.94^{+0.12}_{-0.13}$	$101.54^{+0.15}_{-0.12}$
$0.242^{+0.019}_{-0.010}$	$0.2429^{+0.0070}_{-0.0055}$
$0.582^{+0.046}_{-0.028}$	$0.596^{+0.037}_{-0.029}$
$0.511^{+0.020}_{-0.023}$	$0.512^{+0.007}_{-0.026}$
$0.411^{+0.014}_{-0.022}$	$0.405^{+0.011}_{-0.013}$
$1.000^{+0.087}_{-0.094}$	$0.995^{+0.032}_{-0.044}$
1 (fixed)	1 (fixed)
0 (fixed)	0 (fixed)
$0.0001002^{+0.0000049}_{-0.0000035}$	$0.0001000^{+0.0000040}_{-0.0000025}$
$0.0001005^{+0.0000043}_{-0.0000029}$	$0.0001024^{+0.0000045}_{-0.0000030}$
$1.249^{+0.057}_{-0.029}$	$1.230^{+0.035}_{-0.024}$
1 (fixed)	1 (fixed)
0 (fixed)	0 (fixed)
$0.00136^{+0.00014}_{-0.00005}$	$0.001351^{+0.000036}_{-0.000047}$
$-0.000495^{+0.000016}_{-0.000030}$	$-0.000485^{+0.000033}_{-0.000016}$
0 (fixed)	0 (fixed)
0 (fixed)	0 (fixed)
$4.7043515^{+0.0000012}_{-0.0000017}$	$4.7043516^{+0.0000014}_{-0.0000016}$
$2456705.560361^{+0.000075}_{-0.000069}$	$2456705.560371^{+0.000086}_{-0.000072}$
0.03 ± 0.15	$-0.03^{+0.14}_{-0.10}$

Note.
[a] We believe that star spots must be located on the primary component due to the behavior of F between seasons. We utilize $L_3 = 0.01$ as an upper limit on the third-light contamination and it is likely that L_3 is much less than 0.01. Of these four models, we believe the first column (Prim. spots, $L_3 = 0$) to be the most likely scenario.

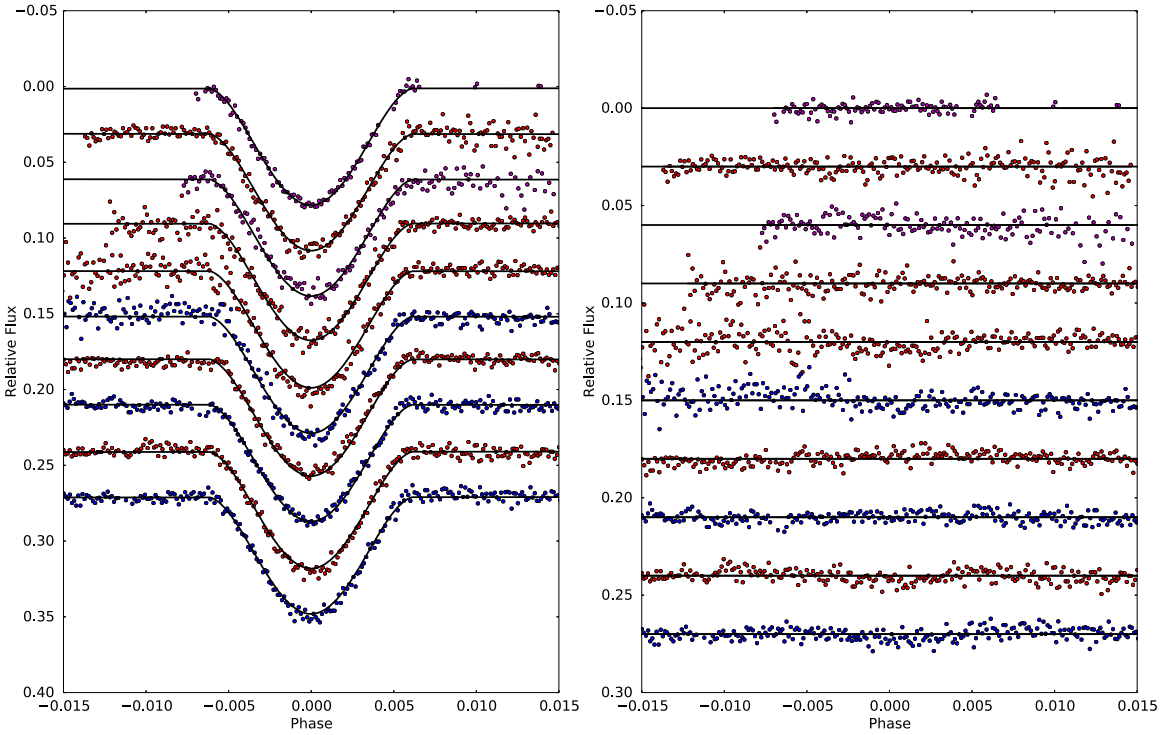

Figure 4. Photometric data of all primary eclipses (offset for clarity) from the 2014–2015 observing seasons and our model with star spots located on the primary component. We have corrected the data for normalization, meridian offsets, and common mode, which are known systematics in the MEarth data. Residuals are located in the lower plot. Each color represents data taken from a different MEarth-south telescope.

Table 7
Physical Parameters of LP 661-13

Parameter	Value	Source
M_1 ($M_\odot$)	0.30795 ± 0.00084	This work
M_2 ($M_\odot$)	0.19400 ± 0.00034	This work
R_1 ($R_\odot$)	0.3226 ± 0.0033	This work
R_2 ($R_\odot$)	0.2174 ± 0.0023	This work
V	14.03	Reid et al. (2004)
R	12.75	Reid et al. (2004)
I	11.17	Reid et al. (2004)
J	9.63 ± 0.02	Skrutskie et al. (2000)
H	9.07 ± 0.02	Skrutskie et al. (2000)
K_s	8.76 ± 0.02	Skrutskie et al. (2000)
Spectral Type	M3.5	Reid et al. (2004)
NIR Spectral Type	M4.27	Terrien et al. (2012)
Distance (pc)	24.9 ± 1.3	This work
Proper motion (R.A., mas yr^{-1})	75.1 ± 2.0	This work
Proper motion (Decl., mas yr^{-1})	−227.3 ± 2.0	This work
γ (km s^{-1})	−0.009 ± 0.014	This work
Period (days)	$4.7043512^{+0.0000013}_{-0.0000010}$	This work
Epoch of primary eclipse (HJD)	$2456705.560353^{+0.000038}_{-0.000040}$	This work
[Fe/H]	−0.07	This work

orbital period (4.704 days). This rotational frequency is consistent between observation seasons when we assume the stellar star spots producing this signal are distributed on the primary star.

4.1. Third Light

Archival SuperCOSMOS images (see Figure 1) indicate that there is a faint background star currently in the MEarth aperture for LP 661-13. This third light can potentially limit our ability to measure the fundamental parameters of each component in this system. The SuperCOSMOS catalog measures this background star to be 5.3 magnitudes fainter than LP 661-13 in the 103a-E red plate bandpass. Unfortunately, we do not know the color of the background star and therefore do not know the magnitude difference in the MEarth bandpass. While it is unlikely that the background star is as red as LP 661-13, we can measure the maximum possible effect that third-light contamination has on the determination of LP 661-13's physical parameters by repeating our analysis with third light fixed (arbitrarily) at 1% of the total light of the system. In Tables 6 and 7, we list the system parameters jointly fitting both seasons of data for third light, $L_3 = 0$ and 0.01 for models with star spots only on the primary stellar component, and for star spots only on the secondary stellar component. The most likely physical scenario is one where the stars pots are concentrated on the more luminous primary and that third light is insignificant for this system. We find that with 1% third-light contamination, the radius of each component of LP 661-13 is affected at the 0.5% level, and therefore we do not believe third light to be a significant concern for this system.

5. Discussion

We have measured the masses of the primary and secondary components of LP 661-13 to a precision of 0.27% and 0.17% and the radii to 1.0% and 1.4%, respectively. At the photon noise limit, the ratio of the standard deviation of the residuals of our spectroscopic orbit scales inversely with the light ratio

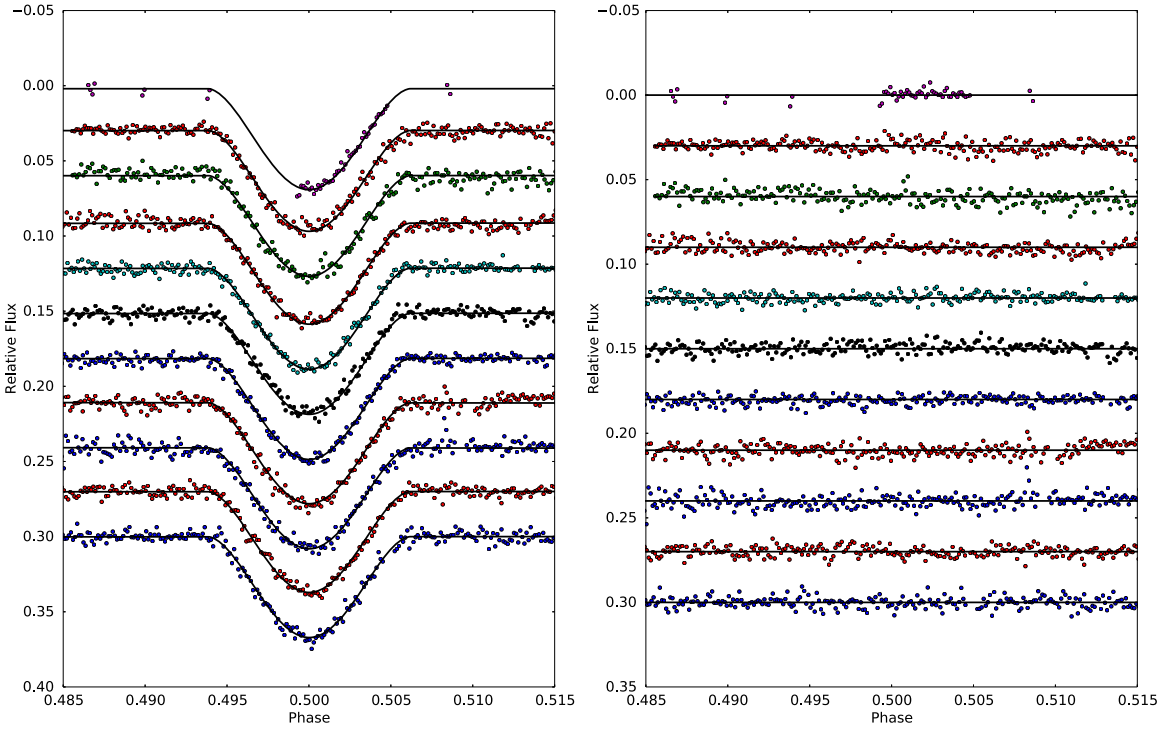

Figure 5. Photometric data of all secondary eclipses (offset for clarity) from the 2014–2015 observing seasons. The partial secondary eclipse was data taken before we knew the period of the LP 661-13 system. MEarth-south automatically detected an event-in-progress and began collecting high cadence follow-up observations until the event ended before resuming normal operations. The colors correspond to the same telescopes as in Figure 4. Residuals from the fit are shown in the lower panel.

(Goldberg et al. 2002). However, in our case, the ratio of our residuals is 0.25, significantly lower than our measured light ratio $L_2/L_1 = 0.434 \pm 0.025$, implying a significant red-noise component in one or both component RV measurements. We further find that a systematic noise floor, present in both components and of the same magnitude, is unable to account for the internal error bars of our component masses. We do not believe this excess noise significantly affects our results, and we note that our determination of the stellar radii of both components is more uncertain than the masses.

The error in the radii is dominated by the systematics associated with the star spots, and further seasons of data will aid in reducing these errors. Particularly, if the star-spot signal changes significantly between seasons, this will aid our ability to break the degeneracies of this model. In future seasons, LP 661-13 will achieve wider separation with the background star, allowing us to measure its color and assess its third-light contribution.

In a previous work (Dittmann et al. 2016), we have shown that the absolute K_s magnitude and the $MEarth - K_s$ color of a mid-to-late M dwarf can be an indicator of the star's metallicity. Here, we have measured the light ratio of both component stars in the MEarth bandpasses, allowing us to separate the *MEarth* magnitude into magnitudes for each star. While we do not have a similar measurement in the K_s band, we can use our measured masses and the mass–luminosity relation from Delfosse et al. (2000) to separate the K_s magnitude into the magnitudes of each component and our trigonometric parallax to convert to an absolute magnitude. We estimate that the metallicity of the primary star is $[\mathrm{Fe/H}] = 0.0$ and the metallicity of the secondary star is $[\mathrm{Fe/H}] = -0.13$, with a precision of approximately 0.1 dex, though this estimate inherits the precision and biases of the relation in Delfosse et al. (2000). We do not believe that the stars in this system formed from different metallicity bulk material, nor that the difference in our two estimates are not significant. We average these two values as our metallicity estimates for the system.

Interestingly, the orbit of this system is circular while at least one of the components is not rotating synchronously with the orbit. However, tidal theory suggests that the timescale for synchronous rotation is much shorter than the timescale for circularization (Habets 1987), so it is unclear how this system can currently be in the state that we observe it in unless it formed in a nearly circular orbit and the system age is smaller than the synchronous rotation timescale.

With these measurements in hand, we can now use these stars as tests of stellar models. In Figure 7, we plot the masses and radii for other low-mass EB systems, along with the stellar models of Baraffe et al. (2015) for a 5 Gyr system of solar metallicity. A table of the values for stars used in this plot is available in Table 8. We find that each of the individual components of LP 661-13 are higher than, but marginally compatible with, the most recent stellar models. We note that the primary component is more inflated than the secondary component and we have determined that it is likely that the rotational modulation from the presence of star spots is likely originating from this component as well. Therefore, it is possible that at least some of this radius inflation is due to the effects of star spots and magnetic activity on the primary component, though we cannot determine how much inflation is caused by this effect.

In EB observations, the sum of the component radii are better determined than each individual component's radius, thus we can investigate whether this radius sum is significantly higher than that expected from stellar models. This also allows us to utilize the precision of our mass measurements in order to fully leverage the available data and test these models. We find that, given the measured stellar masses of $0.308\,M_\odot$ and

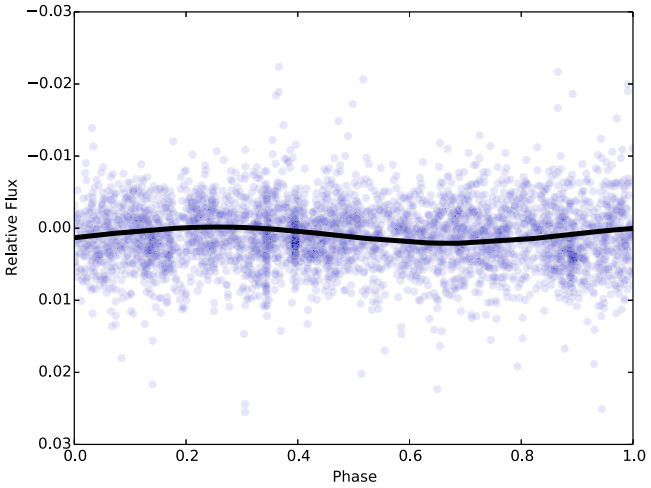

Figure 6. Out-of-eclipse observations of LP 661-13 taken over both observing seasons. We find a rotational modulation signal from longitudinally asymmetrically distributed star spots with a period of 3.856 days, slightly shorter than the orbital period of the system. Since this system is not tidally locked, different star-spot groups are visible during each eclipse. This allows us to constrain the uncertainties on some of our physical parameters.

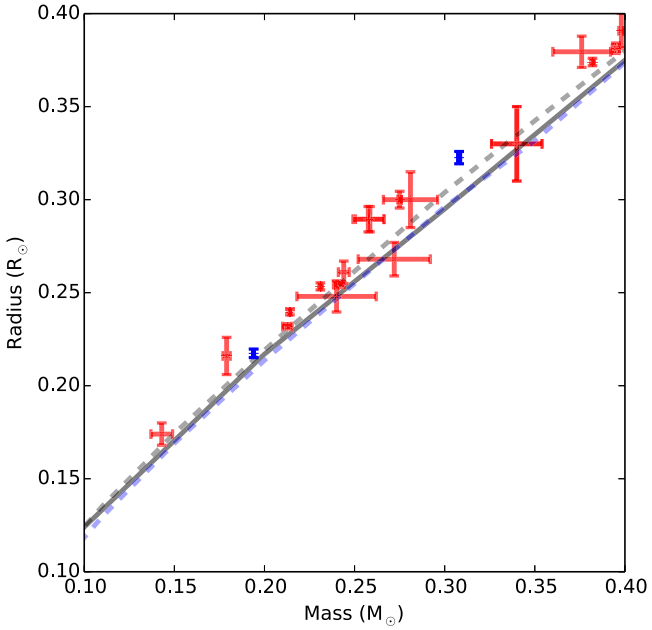

Figure 7. Masses and radii for nearby double-lined low-mass eclipsing binary stars with precise measurements (see Table 8). The fully convective boundary is at 0.35 $M_\odot$. We plot SDSS-MEB-1 (Blake et al. 2008), GJ 3236 (Irwin et al. 2009), CM Dra (Morales et al. 2009), LP 133-373 (Vaccaro et al. 2007), MG1-2056316 (Kraus et al. 2011), KOI-126 (Carter et al. 2011), CU Cnc (Ribas 2003), 1RXSJ154727 (Hartman et al. 2011), HATS551-027 (Zhou et al. 2015b), LSPM J1112+7626 (Irwin et al. 2011), and WTS19g-4-02069 (Nefs et al. 2013) in red. LP 661-13 A and B are indicated by the dark blue crosses. The black line is the stellar model from Baraffe et al. (2015) for a 5 Gyr system with solar metallicity. The black dashed line is for a solar metallicity system with an age of 10 Gyr from the models of Chabrier & Baraffe (1997), while the dashed blue line is for the 10 Gyr, [Fe/H] = −0.5 model from Chabrier & Baraffe (1997). We find that in aggregate the stellar models tend to underpredict the radius for a star of a given mass. While the radius for each component of LP 661-13 is marginally consistent with the stellar models, we find that the much better constrained radius sum is significantly inflated compared to that predicted by the stellar model.

0.194 $M_\odot$, we expect a total radius sum of 0.510 ± 0.005 $R_\odot$. The measured radius sum, 0.536 ± 0.006 $R_\odot$ lies 5% above the model value, implying a significant radius inflation at 4σ confidence.

One of the most straightforward ways in which an M dwarf might be inflated is due to youth. M dwarfs take significantly longer to settle onto the main-sequence than solar-type stars, and may maintain significantly larger radii for up to a billion years. If LP 661-13 is relatively young, we might expect both components to be slightly inflated. We find no evidence for lithium in either component in our measured spectra, which can set a lower limit on their age. However, since both stars are fully convective ($M < 0.35\,M_\odot$, Chabrier & Baraffe 1997), any Lithium originally present in the star would be convected into the interior and destroyed in approximately 10 Myr (Baraffe et al. 2015). Using the stellar models from Baraffe et al. (2015), we find that in order to reproduce the radius sum that we measure, LP 661-13 would need to be approximately 200 Myr old. At an age of 200 Myr, we would expect an X-ray luminosity of $10^{28.5}$ erg s^{-1} (Rebolo & Zapatero-Osorio 2000), which we can rule out with the *ROSAT* data. Furthermore, we find no detectable eccentricity in the system and the circularization timescale is 4.3 Gyr. Therefore, we find it unlikely that the average inflation of these stars can be explained through youth and that it is likely that LP 661-13 is a field age system.

Another possible mechanism that may be responsible for M dwarfs' inflated radii is the presence of metals in the atmosphere. The presence of metals and the cool temperatures present in the atmospheres are conducive to the formation of molecules. In turn, these molecules act as a significant source of opacity in the optical, suppressing the amount of energy that is emitted in these frequency bands. To compensate for this, the star emits significantly more light in the infrared than in the optical compared to a blackbody spectrum. However, it is possible that the star may also expand slightly to have a greater surface area from which to emit the energy it is producing in the stellar interior. In this case, the presence of more metals would lead to a slightly larger radius than for a star depleted in metals. While the new stellar models published by Baraffe et al. (2015) are not computed over a range of different metallicities, previous versions of these models (Baraffe et al. 1998), found that metallicity can only account for a 3% increase in the radius from [Fe/H] = −0.5 to [Fe/H] = 0.0. Since the average radius inflation for LP 661-13 is higher than this, it is unlikely that metallicity can fully account for the discrepancy from the stellar models, and there is likely still theoretical considerations to be addressed to fully understand the mass–radius relation of low-mass stars.

6. Conclusions

We present here the discovery and analysis of the eclipsing M dwarf—M dwarf binary LP 661-13. We have collected two years of eclipse data and precise RV measurements of both components in order to obtain accurate, model-independent measurements of their masses and radii. We find that LP 661-13A is a 0.30795 ± 0.00084 $M_\odot$ star with a 0.3226 ± 0.0033 $R_\odot$ radius, while LP 661-13B is a 0.19400 ± 0.00034 $M_\odot$ star with a 0.2174 ± 0.0023 $R_\odot$ radius. Both components are slightly inflated in radius when compared to stellar models. However, the radius sum (which is much better constrained) is significantly (4σ) inflated when compared to the expected radius sum from stellar models. Because the orbit of the system is circularized, it is

Table 8
Measured Masses and Radii for Low-mass Stars in Eclipsing Binary Systems

Star	Mass ($M_\odot$)	Radius ($R_\odot$)	Source
CMDraA	0.2310 ± 0.0009	0.2534 ± 0.0019	Morales et al. (2009)
CMDraB	0.2141 ± 0.0010	0.2396 ± 0.0015	Morales et al. (2009)
CU CncB	0.3980 ± 0.0014	0.3908 ± 0.0094	Ribas (2003)
GJ3236A	0.376 ± 0.016	0.3795 ± 0.0084	Irwin et al. (2009)
GJ3236B	0.281 ± 0.015	0.300 ± 0.015	Irwin et al. (2009)
HATS551-027A	0.244 ± 0.003	0.261 ± 0.006	Zhou et al. (2015b)
HATS551-027B	0.179 ± 0.002	0.216 ± 0.010	Zhou et al. (2015b)
KOI126B	0.2413 ± 0.0030	0.2543 ± 0.0014	Carter et al. (2011)
KOI126C	0.2127 ± 0.0026	0.2318 ± 0.0013	Carter et al. (2011)
LSPM J1112+7626A	0.395 ± 0.002	0.3814 ± 0.0028	Irwin et al. (2011)
LSPM J1112+7626B	0.275 ± 0.001	0.3000 ± 0.0045	Irwin et al. (2011)
LP133-373A	0.340 ± 0.014	0.33 ± 0.02	Vaccaro et al. (2007)
LP133-373B	0.340 ± 0.014	0.33 ± 0.02	Vaccaro et al. (2007)
LP 661-13A	0.30795 ± 0.00084	0.3226 ± 0.0033	This work
LP 661-13B	0.19400 ± 0.00034	0.2174 ± 0.0023	This work
MG1-2056316B	0.382 ± 0.001	0.374 ± 0.002	Kraus et al. (2011)
1RXSJ154727.5+450803A	0.2576 ± 0.0085	0.2895 ± 0.0068	Hartman et al. (2011)
1RXSJ154727.5+450803B	0.2585 ± 0.0080	0.2895 ± 0.0068	Hartman et al. (2011)
SDSS-MEB-1A	0.272 ± 0.020	0.268 ± 0.009	Blake et al. (2008)
SDSS-MEB-1B	0.240 ± 0.022	0.248 ± 0.0084	Blake et al. (2008)
WTS19g-4-02069A	0.53 ± 0.02	0.51 ± 0.01	Nefs et al. (2013)
WTS19g-4-02069B	0.143 ± 0.006	0.174 ± 0.006	Nefs et al. (2013)

unlikely that this inflation can be explained through youth. Metallicity is also insufficient to explain the total radius inflation we observe.

In the future, the most straightforward way to improve the measurements of this system is to continue out-of-eclipse monitoring and obtain additional eclipse observations. Because we have observed some spot evolution between observing seasons, additional evolution will help to break the degeneracies between star-spot coverage and inferred stellar radii in the model and provide better constraints on the fundamental parameters of this system. Additionally, we can potentially probe the origin of the radius inflation by investigating the marginal X-ray activity as seen by *ROSAT* and attempt to measure its surface magnetic field. Eclipse measurements in other photometric bandpasses will allow us, with the trigonometric parallax distance we have in hand, to measure the effective temperatures of each component as well, which will serve as another test of stellar models. LP 661-13 represents another low-mass stellar test case measured with high accuracy and will be a useful benchmark for current and future stellar models. LP 661-13 is positioned equatorially on the sky and therefore is a good object for further study from both northern and southern facilities.

We thank the anonymous referee for insights and suggestions while reviewing this manuscript. The MEarth Team gratefully acknowledges funding from the David and Lucille Packard Fellowship for Science and Engineering (awarded to D.C.). This material is based upon work supported by the National Science Foundation under grants AST-0807690, AST-1109468, AST-1004488 (Alan T. Waterman Award), and AST-1616624. This publication was made possible through the support of a grant from the John Templeton Foundation. The opinions expressed in this publication are those of the authors and do not necessarily reflect the views of the John Templeton Foundation. E.R.N. was supported by the NSF Graduate Research Fellowship. This research has made extensive use of NASAs Astrophysics Data System (ADS), and the SIMBAD database, operated at CDS, Strasbourg, France.

References

Allard, F., Hauschildt, P. H., Alexander, D. R., Tamanai, A., & Schweitzer, A. 2001, ApJ, 556, 357
Baraffe, I., Chabrier, G., Allard, F., & Hauschildt, P. H. 1998, A&A, 337, 403
Baraffe, I., Homeier, D., Allard, F., & Chabrier, G. 2015, A&A, 577, A42
Berta, Z. K., Irwin, J., & Charbonneau, D. 2013, ApJ, 775, 91
Blake, C. H., Torres, G., Bloom, J. S., & Gaudi, B. S. 2008, ApJ, 684, 635
Boyajian, T., von Braun, K., Feiden, G. A., et al. 2015, MNRAS, 447, 846
Buchhave, L. A., Bakos, G. Á., Hartman, J. D., et al. 2010, ApJ, 720, 1118
Carter, J. A., Fabrycky, D. C., Ragozzine, D., et al. 2011, Sci, 331, 562
Chabrier, G., & Baraffe, I. 1997, A&A, 327, 1039
Claret, A. 2000, yCat, 336, 31081
Davenport, J. R. A., Hebb, L., & Hawley, S. L. 2015, ApJ, 806, 212
Delfosse, X., Forveille, T., Ségransan, D., et al. 2000, A&A, 364, 217
Dittmann, J. A., Irwin, J. M., Charbonneau, D., & Berta-Thompson, Z. K. 2014, ApJ, 784, 156
Dittmann, J. A., Irwin, J. M., Charbonneau, D., & Newton, E. R. 2016, ApJ, 818, 153
Doyle, L. R., Carter, J. A., Fabrycky, D. C., et al. 2011, Sci, 333, 1602
Eggen, O. J., & Sandage, A. 1967, ApJ, 148, 911
Feiden, G. A., & Chaboyer, B. 2014a, in IAU Symp. 302, Magnetic Fields throughout Stellar Evolution, ed. P. Petit, M. Jardine, & H. C. Spruit (Paris: IAU) 150
Feiden, G. A., & Chaboyer, B. 2014b, ApJ, 789, 53
Feiden, G. A., & Chaboyer, B. 2014c, A&A, 571, A70
Foreman-Mackey, D., Hogg, D. W., Lang, D., & Goodman, J. 2013, PASP, 125, 306
Goldberg, D., Mazeh, T., Latham, D. W., et al. 2002, AJ, 124, 1132
Gómez Maqueo Chew, Y., Morales, J. C., Faedi, F., et al. 2014, A&A, 572, A50

Habets, G. M. H. J. 1987, in Cool Stars, Stellar Systems and the Sun, ed. J. L. Linsky & R. E. Stencel (Berlin: Springer), 220
Hartman, J. D., Bakos, G. Á., Noyes, R. W., et al. 2011, AJ, 141, 166
Irwin, J., Charbonneau, D., Berta, Z. K., et al. 2009, ApJ, 701, 1436
Irwin, J. M., Berta-Thompson, Z. K., Charbonneau, D., et al. 2015, in Cambridge Workshop on Cool Stars, Stellar Systems, and the Sun 18, ed. G. T. van Belle & H. C. Harris (Melville, NY: AIP), 767
Irwin, J. M., Quinn, S. N., Berta, Z. K., et al. 2011, ApJ, 742, 123
Irwin, M. J. 1985, MNRAS, 214, 575
Kirkpatrick, J. D., Henry, T. J., & McCarthy, D. W., Jr. 1991, ApJS, 77, 417
Kraus, A. L., Tucker, R. A., Thompson, M. I., Craine, E. R., & Hillenbrand, L. A. 2011, ApJ, 728, 48
Lacy, C. H. 1977, ApJ, 218, 444
MacDonald, J., & Mullan, D. J. 2012, MNRAS, 421, 3084
Mandel, K., & Agol, E. 2002, ApJL, 580, L171
Mann, A. W., Feiden, G. A., Gaidos, E., Boyajian, T., & von Braun, K. 2015, ApJ, 804, 64
Metcalfe, T. S., Mathieu, R. D., Latham, D. W., & Torres, G. 1996, ApJ, 456, 356
Morales, J. C., Ribas, I., Jordi, C., et al. 2009, ApJ, 691, 1400
Mullan, D. J., & MacDonald, J. 2001, ApJ, 559, 353
Nefs, S. V., Birkby, J. L., Snellen, I. A. G., et al. 2013, MNRAS, 431, 3240
Nidever, D. L., Marcy, G. W., Butler, R. P., Fischer, D. A., & Vogt, S. S. 2002, ApJS, 141, 503
Nutzman, P., & Charbonneau, D. 2008, PASP, 120, 317
Popper, D. M., & Etzel, P. B. 1981, AJ, 86, 102
Rebolo, R., & Zapatero-Osorio, M. 2000, Very Low-Mass Stars and Brown Dwarfs, Cambridge Contemporary Astrophysics (Cambridge: Cambridge Univ. Press)
Reid, I. N., Cruz, K. L., Allen, P., et al. 2004, AJ, 128, 463
Ribas, I. 2003, A&A, 398, 239
Salim, S., & Gould, A. 2003, ApJ, 582, 1011
Schwamb, M. E., Orosz, J. A., Carter, J. A., et al. 2013, ApJ, 768, 127
Skrutskie, M. F., Schneider, S. E., Stiening, R., et al. 2000, yCat, 2241, 0
southworth, J. 2013, A&A, 557, A119
southworth, J., Maxted, P. F. L., & Smalley, B. 2004, MNRAS, 351, 1277
Terrien, R. C., Mahadevan, S., Bender, C. F., et al. 2012, ApJL, 747, L38
Torres, G. 2013, AN, 334, 4
Torres, G., Andersen, J., & Giménez, A. 2010, A&ARv, 18, 67
Vaccaro, T. R., Rudkin, M., Kawka, A., et al. 2007, ApJ, 661, 1112
Voges, W., Aschenbach, B., Boller, T., et al. 2000, IAUC, 7432
Zhou, G., Bayliss, D., Hartman, J. D., et al. 2015a, MNRAS, 451, 2263
Zhou, G., Bayliss, D., Hartman, J. D., et al. 2015b, MNRAS, 451, 2263
Zucker, S., & Mazeh, T. 1994, ApJ, 420, 806